J Appl Electrochem (2012) 42:827–832
DOI 10.1007/s10800-012-0441-1

ORIGINAL PAPER

Sonochemical synthesis of Pt-doped Pd nanoparticles with enhanced electrocatalytic activity for formic acid oxidation reaction

Md. Abdul Matin · Ji-Hoon Jang · Eunjik Lee · Young-Uk Kwon

Received: 26 March 2012 / Accepted: 19 June 2012 / Published online: 3 July 2012

Abstract Pt-doped Pd nanoparticle catalysts (Pd_nPt, n is 12, 15 and 19) supported on carbon were synthesized by an ultrasound assisted polyol method. The catalysts were characterized by X-ray diffraction, transmission electron microscopy, and energy dispersive X-ray spectroscopy. The electrochemical activity of the electrocatalysts was investigated in terms of formic acid oxidation reaction (FAOR) at low concentration of formic acid in 0.1 M perchloric acid at room temperature. Formic acid oxidation on the Pd_nPt/C commences at lower potential than a commercial Pt/C. $Pd_{19}Pt/C$ catalyst showed the highest catalytic activity in FAOR compared to that of other catalysts. The obtained electrochemical results from voltammograms indicate that Pt-doped Pd catalysts can be a promising candidate for the anode material in direct formic acid fuel cells. The synthesis procedure is not only a very facile route but also a mass producible method for preparing carbon supported alloy nanoparticles.

Keywords Palladium · Platinum · Electrocatalysts · Sonochemistry · Formic acid oxidation

Md. A. Matin · Y.-U. Kwon
Department of Chemistry, Sungkyunkwan University, Suwon 440-746, Korea

J.-H. Jang · Y.-U. Kwon
Center for Human Interface Nano Technology, Sungkyunkwan University, Suwon 440-746, Korea

E. Lee · Y.-U. Kwon (✉)
SKKU Advanced Institute of Nanotechnology, Sungkyunkwan University, Suwon 440-746, Korea
e-mail: ywkwon@skku.edu

1 Introduction

Fuel cells (FCs) have been considered as an important power source in the future because of their high energy conversion efficiency and environmental soundness [1–3]. Among the various types of FCs, direct formic acid fuel cells (DFAFCs) have been intensively studied because of their high energy density, safety of fuels, and facile system integration for micro-power energy strategy [4–7]. The paucity of appropriate catalysts with high catalytic activity for the formic acid oxidation reaction (FAOR) and good stability against poisoning has been the major hurdle for successful commercialization of DFAFCs [8]. Platinum and palladium have been well known electrocatalysts for the oxidation reactions of small organic molecules such as in FAOR [9–11]. Especially, Pt is the liveliest element for the adsorption of formic acid. However, CO-poisoning is a serious problem with Pt [12]. Therefore, it is an exigent task to develop alternative catalysts to replace pure Pt [13].

The mechanism of electrocatalytic FAOR has not yet been fully understood. However, it is well agreed that FAOR generally occurs by either of the following two pathways [1, 14, 15].

Direct oxidation pathway (dehydrogenation):

$$HCOOH \rightarrow HCOO_{ads} + H^+ + e^-$$

$$HCOO_{ads} \rightarrow CO_2 + H^+ + e^-$$

Indirect oxidation pathway (CO-intermediate):

$$HCOOH \rightarrow CO_{ads} + H_2O \rightarrow CO_2 + 2H^+ + 2e^-$$

In the direct oxidation pathway, the formation of CO_2 occurs without passing a chemisorbed CO-intermediate. In case of indirect oxidation pathway, formic acid is oxidized through a chemisorbed CO-intermediate. The fact that Pt is

poisoned by CO suggests the indirect oxidation pathway for Pt catalysts. On the contrary, Pd or Pd-based electrocatalysts, which are also reported to be FAOR active, are believed to follow the direct oxidation pathway with no intermediate formed [16–18]. Hence, incorporation of Pd into Pt may be a way to achieve poison-tolerant and highly active FAOR catalysts [18, 19]. Indeed, Clavilier and colleagues [20] discovered poisoning tolerant property of Pd deposited on Pt (100) single crystal surface and Yang and colleagues [21] reported that Pd overgrowth on the (100) facets of Pt nanocubes enhanced FAOR. Recently, Zhang et al. [22] synthesized a series of Pd_xPt_{1-x} catalysts and found synergistic effects between Pt and Pd depending on the Pt/Pd ratio. According to their results, the highest performance is achieved with a Pd-rich composition, $Pt_{0.1}Pd_{0.9}$.

In general, the synthesis procedures for bimetallic nanoparticles are time consuming often in multiple steps. In this regard, we reported that sonochemical synthesis can be simpler and faster than the conventional ones [23]. Moreover, this method, sometimes, provides a means to control the elemental distribution within the resultant nanoparticles and hence, different performance of the catalysis of the nanoparticles from those by other synthesis methods. In this study, in order to see the effect of elemental distribution, we applied the sonochemical method to synthesize Pt-doped Pd electrocatalysts supported on carbon for FAOR.

2 Experimental section

Pt-doped Pd catalysts were prepared by the polyol method modified by sonochemistry. Palladium acetylacetonate (Aldrich, $Pd(acac)_2$), platinum acetylacetonate (Aldrich, $Pt(acac)_2$) and Ketjen Black (KB, supplied from SAIT) were added into a three necked flask containing ethylene glycol (30 ml, 99.5 %) which was bubbled under pure Ar prior to the addition. The amount of $Pd(acac)_2$ was fixed and the amount of $Pt(acac)_2$ was varied to make different loaded compositions. Ethylene glycol acts as a reducing agent as well as a mild capping reagent. Ultrasound with 30 % of amplitude of a 500 KW ultrasound generator was applied for 3 h under an Ar-environment. The resultant dark slurry was filtered, washed with ethanol, and then dried under a vacuum for overnight.

The powder X-ray diffraction (XRD) patterns of the samples were obtained with a X-ray diffractometer '[DC/Max 2000, Rigaku, Cu Kα, ($\lambda = 1.54056$ Å)]. The shape and size distribution of the nanoparticles of the samples were studied by a high-resolution transmission electron microscopy (HRTEM, JEOL, JE-3011) at 300 kV. The elemental compositions were obtained by an energy dispersive X-ray spectroscopy (EDS) analyzer attached to a field emission scanning electron microscopy (FESEM, JEOL, JSM-6700F) with a 5,000× magnification.

The electrocatalytic activity was investigated with a potentiostat (Ivium compactstat) and a standard three-electrode electrochemical cell equipped with a glassy carbon rotating disc electrode (RDE, Autolab), a Ag/AgCl reference electrode and a Pt-net counter electrode. 3 mg of the electrocatalyst was dispersed in 1.5 g of distilled water (18.2 MΩ cm). 5 μL of the dispersion was dropped onto the apex of the working electrode ($d = 3$ mm) and then dried in air. 5 μL of 0.05 wt% Nafion solution was applied to cover the electrode material for mechanical protection and dried in air. The working electrode was pretreated electrochemically before each measurement. Cyclic voltammograms (CV) were recorded in a 0.1 M $HClO_4$ aqueous solution at a scan rate of 50 mV s^{-1} under a N_2-environment to characterize the electrocatalysts. The electrocatalytic activity for FAOR was investigated by CV in an electrolyte of 0.1 M $HClO_4$ containing 0.5 M HCOOH under N_2-purging at a scan rate of 50 mV s^{-1}. The reported potentials are referred to the reversible hydrogen electrode (RHE). Two types of current densities, normalized with respect to the electrochemical surface area and the mass of the metal, were calculated and compared.

3 Results and discussion

In this study, we synthesized carbon supported Pd_nPt NPs (Pd_nPt/C, $n = 12$, 15 and 19) using sonochemistry. By varying the amount of the metal precursors in the sonochemical reaction, three samples with different elemental composition were synthesized. The compositions of the NPs synthesized with $Pd(acac)_2$:$Pt(acac)_2$ were determined to be $n = 12$, 15 and 19, respectively, by EDS analyses. Pt-free Pd/C was synthesized by the same method. Pd/C and a commercial Pt/C (TKK, 37.7 wt%) were used as references.

Figure 1 shows the XRD patterns of the Pd_nPt/C samples, Pd/C and Pt/C. The peaks at $2\theta = 40°$, 47°, and 67° are indexed as (111), (200), and (220) reflections of a face centered cubic structure, respectively, and the peak at $2\theta = 26°$ to the carbon support. Because the lattice parameters of Pt (3.920 Å) and Pd (3.908 Å) are close to each other, the peak positions are almost unchanged with the composition. The average particle size, estimated by the Scherrer equation [6], increases as the Pd content increases from 4.7 nm for $Pd_{12}Pt/C$ to 6.8 nm for Pd/C (Table 1).

TEM images of $Pd_{19}Pt/C$ are shown in Fig. 2. The images of $Pd_{12}Pt/C$ and Pd/C are similar except for the different particle sizes. The low magnification image (Fig. 2a) shows well-dispersed NPs on the carbon support. The particle size is in the range between 4 and 12 nm, in

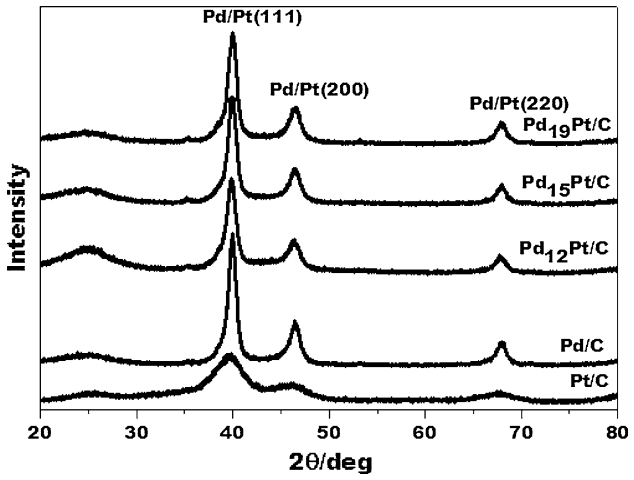

Fig. 1 XRD patterns of the catalysts Pt/C, Pd/C, $Pd_{12}Pt/C$, $Pd_{15}Pt/C$, and $Pd_{19}Pt/C$

good accordance with the XRD result. The NPs have either spherical or triangular shape. The high resolution images of individual NPs, one spherical and the other triangular (Figs. 2b, c), indicate the highly crystalline nature of the NPs. The lattice fringes show (111) planes. There are a few different crystalline domains within each NP, indicating their polycrystalline nature.

Figure 3 compares the CV curves of Pd_nPt/C, Pd/C, and Pt/C, recorded in N_2-saturated 0.1 M $HClO_4$ solutions at room temperature with a scan rate 50 mV s^{-1}. The curve of Pt/C shows a broad peak in the potential range of 0.0–0.3 V for the oxidation of adsorbed hydrogen, characteristic of polycrystalline Pt in the literature [24]. Single crystalline Pd shows a sharp peak at 0.05 V and a broad peak centered at $\sim$0.2 V, which are assigned to the oxidation of hydrogen adsorbed on the (111) and the (100) surfaces, respectively [24]. Zhang et al. [22] found that the peak from the (111) surface is further sharpened and negatively shifted on addition of Pt. At the same time, the peak from the (100) surface decreases in intensity. Although the origin of these observations is not clear, they attribute to the modification of the d-band center by incorporating Pt. Our data also show the sharpening and the negative shift of the peak from the (111) surface in the Pt-containing samples. However, in our case, the peak of $Pd_{19}Pt/C$ is sharper and is more positively shifted than those of $Pd_{12}Pt/C$ and $Pd_{15}Pt/C$, contrary the trend in their paper. In fact, the peak from the (111) surface of $Pd_{12}Pt/C$ is considerably smaller than that of Pd/C. This is partly because the former has smaller particles than the latter. As the particle size becomes small, the fraction of atoms on the facets is drastically reduced. On the contrary, the signal of $Pd_{19}Pt/C$ is heavily concentrated at 0.3 V, suggesting that its NPs have well-developed (111) facets compared with the other samples.

Probably, the different synthesis methods produced different elemental distributions, which can sensitively influence the electrocatalytic behavior. We have formed a model to explain the elemental distribution within NPs synthesized by the sonochemical method [23]. According to this model, the elemental distribution is dependent on the relative vapor pressures of the metal precursors; the more volatile one participates the nuclear formation more than the less volatile one. As a result, the metal of the more volatile precursor is more concentrated in the core part of the NPs and the other more concentrated on the shell. Since $Pd(acac)_2$ has a higher vapor pressure than $Pt(acac)_2$ [23, 25], we expect that the Pt composition is higher on the surface than the averaged composition. By contrast, without the sonication, the reduction reaction of $Pt(acac)_2$ is more favorable than that of $Pd(acac)_2$ and the Pt composition on the shells of NPs by this method is likely to be lower than that of the averaged one.

The electrochemical surface areas (ESA) of the electrode materials are compared in Table 1. These values were obtained by the integration of the curves in the hydrogen desorption region of the CVs with reference to the value of 210 μC cm^{-2} for polycrystalline Pt and Pd

Table 1 Structural, compositional, electrochemical data of Pt-doped Pd nanoparticles

Catalyst	Particle size[a] (nm)	Pd:Pt[b] (atomic ratio)	Metal content[b] (wt%)	Maximum current density (mA mg^{-1} or μA cm^{-2}_{ESA})/peak potential (V)		ESA[c] cm^{-2}
				Forward scan mA mg^{-1}/μA cm^{-2}_{ESA}/V	Backward scan mA mg^{-1}/μA cm^{-2}_{ESA}/V	
Pt/C	3.2	0:100	37.7	118/173/0.56	344/492/0.69	1.6
Pd/C	6.8	100:0	25.2	207/548/0.47	303/797/0.44	0.59
$Pd_{12}Pt/C$	4.7	92:8	23.1	112/609/0.50	191/1056/0.36	0.27
$Pd_{15}Pt/C$	6.1	94:6	24.2	231/936/0.46	332/1327/0.41	0.37
$Pd_{19}Pt/C$	6.2	95:5	30.2	276/1024/0.48	474/1743/0.44	0.48

[a] Calculated by Scherrer equation

[b] From EDS averaged from five different areas of each sample

[c] Calculated by integrating the CV curves in H-active regions

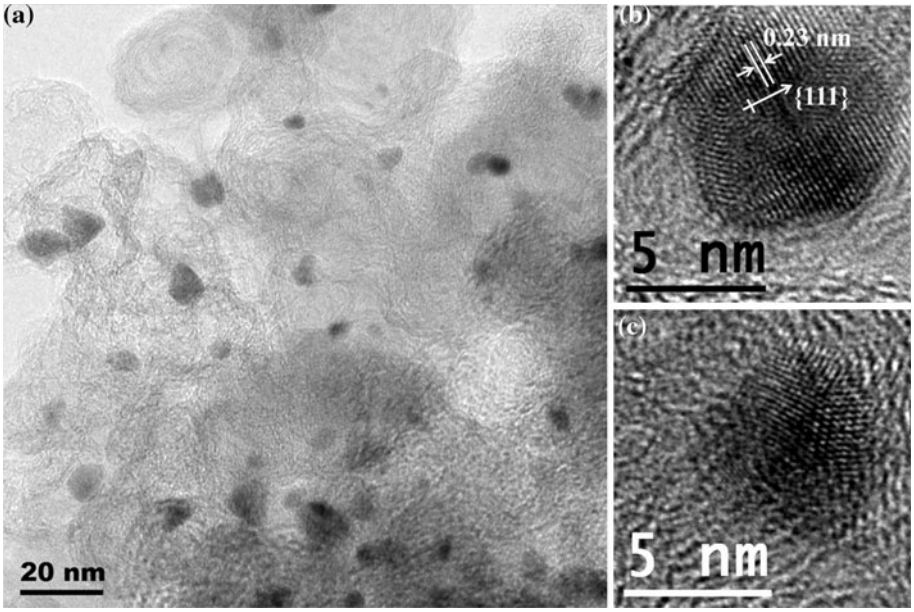

Fig. 2 TEM images of catalyst $Pd_{19}Pt/C$ (**a**) low-magnification image and (**b**) high-magnification image on a spherical NP, and (**c**) high-magnification image on a triangular NP

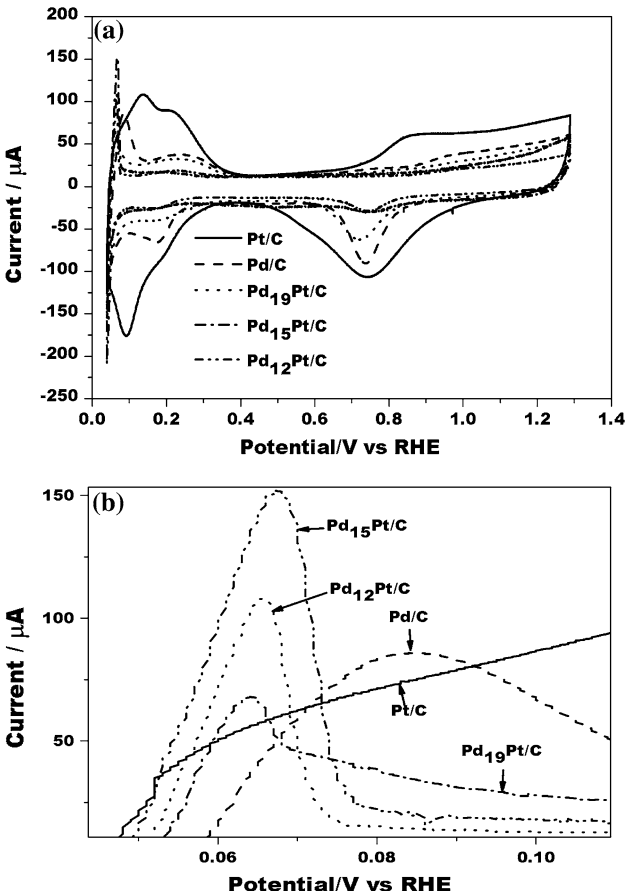

Fig. 3 **a** CVs of the catalysts Pt/C, Pd/C, $Pd_{12}Pt/C$, $Pd_{15}Pt/C$, and $Pd_{19}Pt/C$ measured in N_2-purged 0.1 M $HClO_4$ at room temperature with a scan rate 50 mV s^{-1} and **b** close view of Hydrogen desorption regions of Pt/C, Pd/C, $Pd_{12}Pt/C$, $Pd_{15}Pt/C$, and $Pd_{19}Pt/C$

[26]. The Pt/C has the largest ESA value, probably because its NPs are the smallest. However, one has to be careful in comparing the ESA data among the samples because the metal content varies from sample to sample. Although direct comparison is not possible because of the different particle sizes, these values may be compared after scaled with the metal contents.

Figure 4 displays the CVs of FAOR on the electrocatalysts, measured in N_2 saturated 0.1 M $HClO_4$ electrolytes containing 0.5 M HCOOH at room temperature. The electrochemical data of CV for FAOR are converted into current densities by two normalizing factors; the mass of the catalyst (Fig. 4a) and the ESA (Fig. 4b). For Pt/C, FAOR is strongly inhibited by the CO poisoning and only a weak signal is observed in the forward scan. In the backward scan, FAOR occurs at a higher potential after the CO poison is oxidized and removed from the surface. On the contrary, the CV of Pd/C does not show the signal of CO poisoning in agreement with the literature [21, 22]. Accordingly, the peak potentials for Pd/C (0.47 and 0.44 V in the forward and backward scans, respectively) are considerably lower than those for Pt/C (0.56 and 0.69 V).

The CVs of Pd_nPt/C catalysts show that these are relatively free from the CO poisoning problem, in agreement with the report of Zhang et al. [22]. However, the two samples ($Pd_{19}Pt/C$ and $Pd_{12}Pt/C$) show drastically different catalytic performances. The peak potentials of $Pd_{12}Pt/C$ are slightly higher (0.50 V) in the forward scan and considerably lower (0.36 V) in the backward scan than Pd/C, which may be considered as improvement. However, it shows a large reduction of the peak intensities from that of Pd/C in

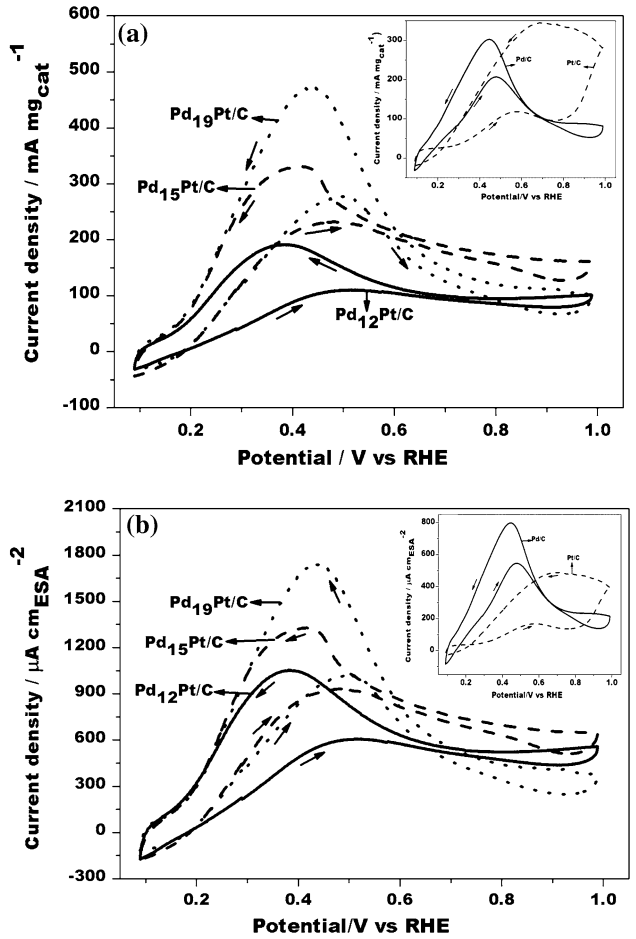

Fig. 4 CVs (10th scan) of the catalysts $Pd_{12}Pt/C$, $Pd_{15}Pt/C$, and $Pd_{19}Pt/C$ measured in N_2-purged 0.1 M $HClO_4$ containing 0.5 M HCOOH at room temperature with a scan rate 50 mV s^{-1}. The plots are scaled to show the current densities normalized with respect to the catalyst mass (**a**) and the electrochemical surface area (**b**). The *insets* are corresponding CVs of Pt/C and Pd/C

the current density plots normalized by the mass of the catalyst (Fig. 4a). Since this sample has a slightly smaller metal content than that of Pd/C, the reduction of peak intensity may be due to the loss of (111) facets by the reduced particle size. On the contrary, $Pd_{19}Pt/C$ shows improved catalytic properties than any other samples. Its FAOR peak potentials are almost the same as those of Pd/C in both the forward and backward scans. However, the peak intensities are increased from those of Pd/C. In the forward scan, the ca. 33 % increased current density may be due to the increased metal loading. In the backward scan, however, the current density is more (56 %) than that of Pd/C, a part of which must be due to the inherent properties (see below) of $Pd_{19}Pt/C$. The trend seen in Fig. 4a is kept unchanged in current densities normalized by ESA (Fig. 4b) although the relative magnitudes are changed. In this plot, the current density of Pt/C appears very small because it has the largest ESA (1.6 cm^{-2}) among the samples. This plot also shows the highest current density for $Pd_{19}Pt/C$. Therefore, based on the two types of current density data, we can conclude that $Pd_{19}Pt/C$ is the most efficient catalyst for FAOR. The electrochemical data are given in Table 1.

The catalytic performance in the Pd–Pt system is bound to be volcanic in nature because the properties of Pd and Pt are complementary and there must be an optimal composition. In their paper, Zhang et al. located the optimal composition at $Pd_{0.9}Pt_{0.1}$; their $Pd_{0.95}Pt_{0.05}$ sample, corresponding to $Pd_{19}Pt/C$ of our data, showed considerably reduced current density from $Pd_{0.9}Pt_{0.1}$. According to their explanation, when two or more Pt atoms in direct neighbors, they catalyze the dehydration of formic acid into CO and the catalyst surface becomes CO-poisoned. Therefore, from the standpoint of suppressing the CO-poisoning, it is desirable to have single Pt atoms fully surrounded by Pd atoms, in which case the direct oxidation of formic acid can take place via the dehydrogenation on the Pt sites. Based on models in which Pt and Pd atoms are statistically distributed, at the $Pd_{0.9}Pt_{0.1}$ composition most of the Pt atoms are separated from the other Pt atoms. In this regards, our results show that the optimal composition is further shifted to the Pd-richer side. As mentioned earlier, the sonochemical synthesis on the system of $Pd(acac)_2$ and $Pt(acac)_2$ has the tendency to concentrate Pt on the surfaces of NPs. Therefore, one can understand the shift of the optimal composition as the different elemental distributions depending on the synthesis method. That is, with the Pt atoms concentrated in the surface, the required amount of Pt to attain the isolated Pt atoms is reduced. In addition, of course, other factors such as the different particles sizes and particle shapes also could contribute to the shift of the optimal composition.

4 Conclusion

In this study, we used a sonochemical method to prepare Pt-doped Pd catalysts. Based on the electrochemical results, the Pt-doped Pd NPs do not show the CO-poisoning problem. $Pd_{19}Pt/C$ showed higher catalytic activity than Pd/C, $Pd_{12}Pt/C$ and $Pd_{15}Pt/C$, different from the literature which located the optimal composition at $\sim Pd_9Pt$. The difference can be explained with the different distribution of Pt and Pd within the NPs depending on the synthesis method. Sonochemistry in this system has the advantage of concentrating the more precious Pt on the surfaces of the NPs, an economic advantage for applications.

Acknowledgments This work was supported by Grants NRF-2011-0031392 (Priority Research Center Program) and NRF-2011-0006268

(Basic Science Research Program). We thank KBSI and CCRF for the TEM and EDS data.

References

1. Zhang S, Shao Y, Yin G, Lin Y (2010) Angew Chem Int Ed 49:2211–2214
2. Huang Y, Zhou X, Liao J, Liu C, Lu T, Xing W (2008) Electrochem Commun 10:621–624
3. Wang X, Xia Y (2008) Electrochem Commun 10:1644–1646
4. Wang R, Liao S, Ji S (2008) J Power Sources 180:205–208
5. Lim B, Yu T, Xia Y (2010) Angew Chem Int Ed 49:9819–9820
6. Liu Z, Hong L, Tham MP, Lim TH, Jiang H (2006) J Power Sources 161:831–835
7. Meng H, Sun S, Masse J-P, Dodelet J-P (2008) J Chem Mater 20:6998–7002
8. Baranova EA, Miles N, Mercier PHJ, Page YL, Patarachao B (2010) Electrochim Acta 55:8182–8188
9. Wang C, Peng B, Xie H-N, Zhang H-X, Shi F-F, Cai W-B (2009) J Phys Chem C 113:13841–13846
10. Ferrando R, Jellinek J, Johnson RL (2008) Chem Rev 108:845–910
11. Selvaraj V, Grace AN, Alagar M, Colloid Interf J (2009) Science 333:254–262
12. Gojkovic SLj, Tripkovic AV, Stevanvic RM, Krstajic NV (2007) Langmuir 23:12760–12764
13. Xu D, Bliznakov S, Liu Z, Fang J, Dimitrov N (2010) Angew Chem Int Ed 49:1282–1285
14. Liu B, Li HY, Die L, Zhang XH, Fan Z, Chen JH (2009) J Power Sources 186:62–66
15. Chen YX, Heinen M, Jusys Z, Behm RJ (2006) Angew Chem Int Ed 45:981–985
16. Yi Q, Huang W, Liu X, Xu G, Zhou Z, Chen A (2008) J Electroanal Chem 619–620:197–205
17. Francisco JV-I, Jose S-G, Herrero E, Aldaz A, Feliu JM (2010) Angew Chem Int Ed 49:6998–7001
18. Wu YN, Liao SJ, Su YL, Zeng JH, Dang D (2010) J Power Sources 195:6459–6462
19. Winjobi O, Zhang Z, Liang C, Li W (2010) Electrochim Acta 55:4217–4221
20. Llorca MJ, Feliu JM, Aldaz A, Clavilier J (1994) J Electroanal Chem 376:151–160
21. Lee H, Habas SE, Somorjai GA, Yang P (2008) J Am Chem Soc 130:5406–5407
22. Zhang H-X, Wang C, Wang J-Y, Zhai J–J, Cai W-B (2010) J Phys Chem C 114:6446–6451
23. Jang J-H, Kim J, Lee Y-H, Kim IY, Park M-H, Yang C-W, Hang S-J, Kwon Y-U (2011) Energy Environ Sci 4:4947–4953
24. Vielstich W, Lamm A, Gasteiger H (eds) (2003) Handbook of fuel cells: fundamentals, technology and applications. Wiley, Chichester
25. Zharkova GI, Stabnikov PA, Sysoev SA, Igumenov IK (2005) J Struct Chem 46(2):320–327
26. Mayrhofer KJJ, Strmcnik D, Blizanac BB, Stamenkovic V, Arenz M, Markovic NM (2008) Electrochim Acta 53:3181–3188